ORIGINAL PAPER

Assessing the impact of flood inundation dynamics on an urban environment

Peng Gao[1] ⬩ **Wei Gao**[2] ⬩ **Nan Ke**[2]

Abstract

This study attempted to examine the complex impact of dynamic inundation process of extreme events on flood hazard assessment (FHA) for the affected urban settings around a local river in New York, USA. Using HEC-RAS 2D, LIDAR DEM, distributed values of surface roughness, and hourly discharges at both ends of the selected reach, we simulated the full inundation process of a 500-year storm event, constructed in terms of the existing largest storm event. We presented flooding status at three flooding moments and quantitatively described the temporal changes of inundation area, depth, and the associated stream power over the entire flood period. Then, we analyzed differences of inundated areas in four classes defined using traditional classification (TC) and process-based classification (PBC). The (static) former was based on the maximum inundation map, while the (dynamic) latter accounted for both inundation depth and duration. We showed that inundated areas in higher classes based on TC were much greater than those in similar classes based on PBC, indicating the significant impact of inundation duration on classification of flood hazard. Next, we investigated the impact of different land use/cover on the difference of inundated areas between the two types of classifications and found that it was complex and displayed no consistent trend from areas surrounding individual buildings (local scale) to large inundated areas (global scale). We emphasize the importance of considering the overall impact of the entire flood processes of an event on future FHA.

Keywords Flood hazard assessment · Inundation process · Inundation duration · Inundation depth · HEC-RAS 2D

1 Introduction

Among natural disasters that greatly disturb human lives, properties, and living environments, flooding receives a top rank because of its worldwide impact and high frequency (Adelekan 2011; Borga et al. 2011; Kvocka et al. 2015; Wahl et al. 2015). It has been well known that climate change and urbanization have increased the frequency and magnitude

✉ Peng Gao
   pegao@syr.edu

1   Department of Geography and the Environment, Syracuse University, Syracuse, NY 13244, USA

2   Department of Remote Sensing, China University of Geosciences, Wuhan, Hubei, China

🖄 Springer

of floods (Li et al. 2013; Rojas et al. 2013; Zhang and Pan 2014; Jenkins et al. 2017). Urbanization reduces permeability of the ground surface, encouraging flashy floods even for regular rainfall events. Global warming that has been confirmed by more and more evidence (IPCC 2013; Liu et al. 2019) increases chances of flashy floods occurring in urban areas of head watersheds by inducing more heavy rainfall and/or unseasonal snowmelt events. Thus, flashy floods tend to occur more frequently around the world (Jonkman 2005; Barredo 2007; Kvocka et al. 2018). The occurrence of flashy floods, which are characterized by fast arrival of the peak discharge (Terti et al. 2015; Bodoque et al. 2016), is not only related to meteorological conditions (e.g., rainfall intensity and air temperature), but also topographical and hydrological settings of the affected areas (Marchi et al. 2010). It follows that flashy floods may be highly variable in space and over time (Marchi, 2009; Aroca-Jimenez et al. 2017), which greatly challenges flood prediction and pre-flood warning. For example, a local watershed of 311 km^2 in central New York had a historical flood event with the recurrence interval (RI) of 86 years, but the flood was caused by a highly concentrated 'regular' rainfall event (RI = 11) (Gao and Hartnett 2016). Therefore, knowledge of degree and extent of flood impact on an urban area is critical for determining mitigation priorities and making flood compensation policies (Darabi et al. 2019). Thus far, these practices are mostly based on assessment of flood risk that involves a combination of flood hazard evaluation and vulnerability analysis (Meyer et al. 2009; De Moel et al. 2015; Sy et al. 2019). Here, we solely focused on the former, which is typically achieved in terms of static flood inundation maps developed using a variety of methods (Link et al. 2019; Abdessamed and Abderrazak 2019; Prabnakorn et al. 2019).

Although approaches involving individual survey and stakeholder collaboration may provide specific information about flood impact on individual urban residents and/or specific groups (Adelekan 2011; Roosa et al. 2017), creation of detailed flood maps indicating different flooding stages is more useful for flood hazard and risk assessment (D'Oria et al. 2019). While inundation extent and depths, flow velocities, and duration time are key parameters for characterizing flooding processes (Gain and Hoque 2013; Arrault et al. 2016), the most commonly used end product is maximum inundation map, which shows the potential extent of flooded water might reach. In Europe, the Flood Directive of the European Commission mandates flood risk maps for all river basins and sub-basins with significant potential risk of flooding (Apel et al. 2009). In the USA, Federal Emergency Management Agency (FEMA) regularly updates insurance maps of all watersheds to provide accurate flood hazard and risk data that may facilitate mitigation actions at all administrative levels (https://www.fema.gov/national-flood-insurance-program-flood-hazard-mapping).

A variety of methods have been proposed to develop these maps. Using available historical maps is a classic approach to delineating inundation extent by comparing maps at different times (Apel et al. 2009; Jalayer 2014). Remote sensing data and GIS technology offer a different means of identifying flood inundation zones (Awadallah and Tabet 2015; Franci et al. 2016; Waghwala and Agnihotri 2019). Yet, the most widely used approach resorts to a variety of hydrodynamic models that may be divided into one-dimensional (1D), two-dimensional (2D), and three-dimensional (3D) models, according to their degrees of complexity in spatially representing the floodplain flow (Schumann et al. 2014; Meesuk et al. 2015; Wang et al. 2015; Alivio et al. 2019). The 1-D models treat flow as the one-dimensional object along the central line of a river channel (DHI 2003; Brunner 2016). They may simulate flow processes in river channels with a low computational cost (Callow and Boggs 2013; Tsakiris 2014), The 2-D models are capable of describing the complex topography of a floodplain and free flow on it (Dottori and Todini 2013; Banks

et al. 2014; Mihu-Pintilie et al. 2019). Despite the ability of representing vertical components of the flood-relevant parameters, 3-D models are unnecessarily complex and require intensive computation (Tsakiris 2014). Limitations of these models have fostered a trend of combining 1D with 2D models, possibly including GIS (Mani et al. 2014; Bisht et al. 2016; Fan et al. 2017), such as MIKE, HEC-RAS, LisFlood-FP, and TUFLOW, which have been corroborated for their robust performance (Yu and Lane 2006; Sanders et al. 2008).

However, majority of model assessments and applications were based on prediction of the flood inundation map showing the (maximum) inundation extent with spatially variable inundation depths (Mason et al. 2009; Sarhadi et al. 2012; Smith et al. 2014; Dimitriadis, 2016; Afshari et al. 2018; Langhammer and Vackova 2018). The implied assumption in these studies was that the most severe damage of flooding was associated with the maximum inundation extent. This may not be true in many cases. For example, a building that was inundated by flow with the depth of 3 m for one hour at the maximum inundation moment may be only inundated by flow with the depth of 1 m for many hours, while the one suffered the maximum inundation depth of 2.5 m might be inundated by the depth of 2 m for a long time period. The flood hazard to the latter could be greater than that to the former. This difference could affect the policy of flood management, which relies on the advance assessments on the flood events. (Meyer et al. 2009). Therefore, understanding dynamics of inundation processes and the associated variable impacts on flood-zone objects, such as buildings, could provide a valuable information for better managing flood disasters. Apparently, this issue has not been well investigated. To fill the gap, this study aimed at (1) characterizing the inundation dynamics of a projected extreme (500-year) flood event in City of Syracuse, New York, (2) developing a process-based classification for more accurate assessment of flood damage, and (3) evaluating the important role of land use/cover (LULC) in the new classification.

Although a number of above-mentioned models are qualified for achieving our purposes, we selected HEC-RAS2D in this study because it directly predicts inundation process in the 2D floodplain. We first calibrated the HEC-RAS2D model using obtained high-resolution DEM data and discharge data of a known rainfall event. Then, we simulated a constructed 500-year event based on recorded historical hydrographs and demonstrated the dynamics of inundation processes and temporal changes of inundation depth, area, and stream power. Next, we quantitatively developed a new classification for assessing flood damage by considering both inundation depths and their durations and demonstrated its differences from the classic classification Third, we examined the variable influences of different LULC types on the new classification. Finally, we showed the potential value of this new classification in assessing flood hazards.

2 Materials and methods

2.1 Study area

Onondaga Creek runs over 43.5 km from its southwest edge bounded by the terminal moraine of glaciers to the north end connecting to Onondaga Lake (Fig. 1). Its downstream reach, which is approximately 11.2 km with no major tributaries, passes through the City of Syracuse (Fig. 1). Although most of the downstream reach has been channelized during the 1963–1969 period (OEI 2009), its neighboring urban area still suffers from flood disasters. According to the historical record, this area experienced 28 flood incidents from
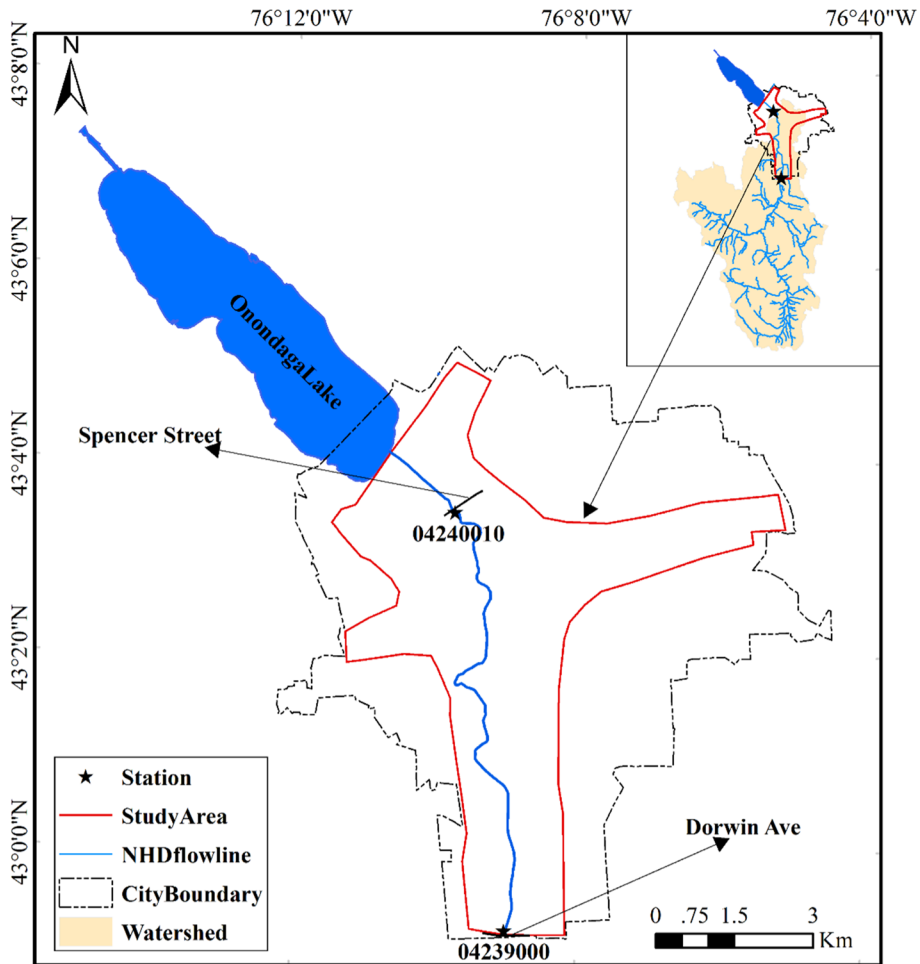
Fig. 1 Geographic setting of the study area. 'Station' refers to locations of the two USGS gauging stations. The yellow area in the inset represents Onondaga Creek watershed, which only covers a proportion of City of Syracuse. 'NHDflowline' denotes the selected downstream reach of the Onondaga Creek

the Onondaga Creek between 1865 and 2007, most of which occurred either in winter or early spring due to unseasoned warm weather (Dormitory Authority of the State of New York 2016; FEMA 2016).The study area includes the neighboring lands around the downstream reach of the Onondaga Creek and the belt extended to the east edge of the city (Fig. 1). It has lower elevations compared with most of other parts in the city and thus represents the city portion that might be inundated by extreme events. Geomorphologically, the study area sets its upstream boundary at Dorwin Avenue on the south and the downstream boundary at the outlet to Onondaga Lake. Selection of this study area was based on three factors. First, urban residents and properties in this area are most vulnerable to the potential flooding. Thus, understanding the potential impact of extreme flood events on such an urban environment not only has a great social and economic significance for local urban residents but also provides a valuable example for other cities suffering similar flooding problems. Second, the selected river reach within the study area includes

two USGS gauging stations, one is on the upstream boundary (04,239,000) and another is at Spencer Street (04,240,010), about 1.8 km upstream of the north boundary of the study area (Fig. 1). Hydrological data available from these two stations allowed us to prepare the input discharge data, calibrate the model, and construct a 500-year event. Third, the selected neighboring area is within the projected inundation zone of a 500-year flood event by Federal Emergency Management Agency (FEMA) (http://fema.maps.arcgis.com/home/webmap/viewer.html?webmap=cbe088e7c8704464aa0fc34eb99e7f30&extent=-76.29363549316382,43.0088974816628,-76.00112450683609,43.09168942623266). Thus, our predicted results may be compared with that from FEMA.

## 2.2 Software for modeling flood dynamic processes

HEC-RAS 2D was used in this study to simulate the hydraulic and hydrological processes of the selected flood events in the study reach of the Onondaga Creek. HEC-RAS, which refers to the Hydrologic Engineering Center's River Analysis System developed by U.S. Army Corps of Engineers, is an integrated software system designed for interactive use in a multi-tasking environment. As an open-source software, HEC-RAS is free downloadable and has 1D and 2D versions, both of which may be used to simulate hydrodynamic processes for flooding events. In the USA, HEC-RAS 1D model has been widely used to create flood risk map by FEMA.

HEC-RAS 2D simulates flow hydrodynamic processes using either 2D diffusion wave equations or full 2D St. Venant equations. The former is a simplified procedure that reduces the complexity of hydrodynamic processes of a flow, while the latter keeps the full scale of its hydrodynamic characteristics. Although the simplified module avoided the demand of high-resolution terrain data, which may not be always available, the full module is preferable for its improvement of modeling accuracy if high-resolution data are available (Dottori and Todini 2011; Tsakiris 2014; Costabile and Macchione 2015). In this study, we adopted the full module for achieving results with higher accuracy.

2.3 Data collection and model setup

Basic input data required for running HEC-RAS 2D are (1) high-resolution DEM representing morphology of the study river channel and its adjacent area; (2) distributed values of surface roughness, which may be assigned using the available land use and land cover (LULC) data; (3) field-observed hydraulic data, which are typically discharge and stage data, as well as channel cross sections. The DEM data for our study area were converted from an available LIDAR (Light Detection and Ranging) data with the resolution of 0.3 m. Because the study area is highly urbanized, many bridges and roads were built cross the selected reach. Therefore, channel morphology in these places cannot be represented by DEM and was estimated based on their neighboring morphology. After this correction, the river channel with variable elevations was topographically connected to the overbank flow areas and the boundary of the 2D flow area for simulation was delineated for use in the subsequent simulation (Fig. 2).

Nonetheless, because LIDAR cannot penetrate into water to detect the true channel bed, the cross sections extracted from LIDAR generally had higher channel beds compared with their counterparts measured in situ. By comparing 9 true cross sections measured by Army Corps and Engineering with the extracted ones from DEM (Fig. 2), we estimated that on
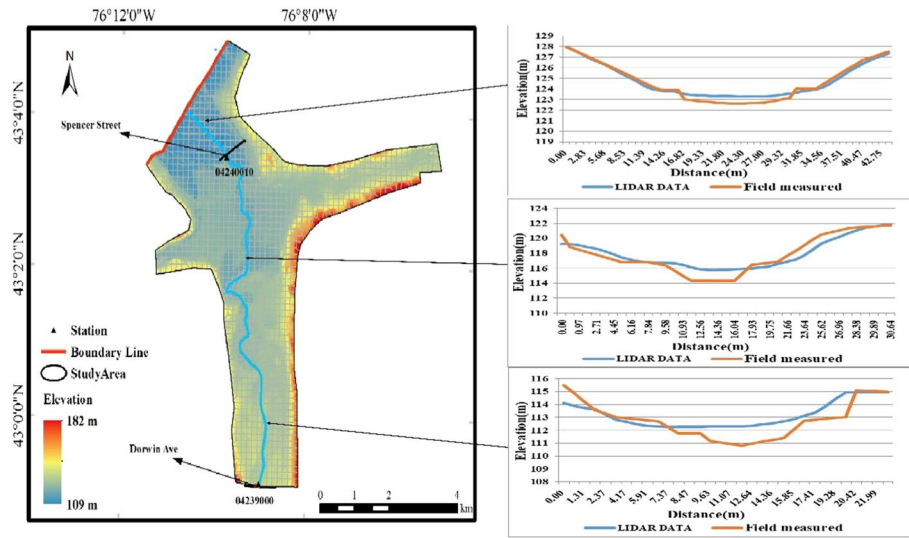
Fig. 2 DEM of the study area with a high resolution (0.3 m), which was divided into a grid of cells with the same size (1 m resolution). The boundary line (red) defines the edge where water flows out of the study area. The three pairs of channel cross sections on the right were examples showing the differences between DEM (blue) and field-measured (orange) data

average the true channel bed is 0.42 m lower than the extracted one. Based on this, the extract channel beds were lowered by the average depth.

To assure the accuracy of the determined values of the spatially distributed surface roughness for improving modeling outcomes, LULC types of the study area were classified using both the 2010 LIDAR data and the 2009 New York State 4-ban leaf-off ortho-photographs. The resultant LULC classes were tree canopy, grass/shrub, water body, bare earth, buildings, roads, and other paved surfaces (University of Vermont Spatial Analysis Laboratory, USDA Forest Service) (Fig. 3a). Their associated roughness values (i.e., Manning's n) were selected in terms of previous studies (Table 1). The values of 0.1 for forest and grass/shrub lands, 0.3 for water body and bare earth, and 0.03 for other paved surface were suggested by both FEMA and O'Brien & Gere in a local flood control project sponsored by City of Syracuse based on their field observation (Dormitory Authority of the State of New York 2016; FEMA 2016). The roughness value for roads was set as 0.016 and for buildings was assigned as 0.4 (Syme 2008; Dorn et al. 2014).

This classification over-simplified variation of surface roughness in channel bed and banks, as well as its vicinity areas because many of these areas are shaded by tree leaves due to high density of plants along the channel. Since a large proportion of the channel within the study area has been artificially protected, the channel was divided into three parts, the bed and low banks covered by water, the upper banks with paved surface, and the overbank areas covered with grass. The roughness value was assigned as 0.03 for the first two and 0.1 for the last one (Table 1). These arrangements finally ended up with a distribution of roughness values in the study area (Fig. 3b).

Discharge and stage data for the selected storm events were downloaded from USGS websites of these two stations. These data were used to establish boundary conditions for model simulation. Different from HEC-RAS 1D, HEC-RAS 2D requires that (i) the 2D flow area should be connected to stream channels and (ii) external boundary conditions should be
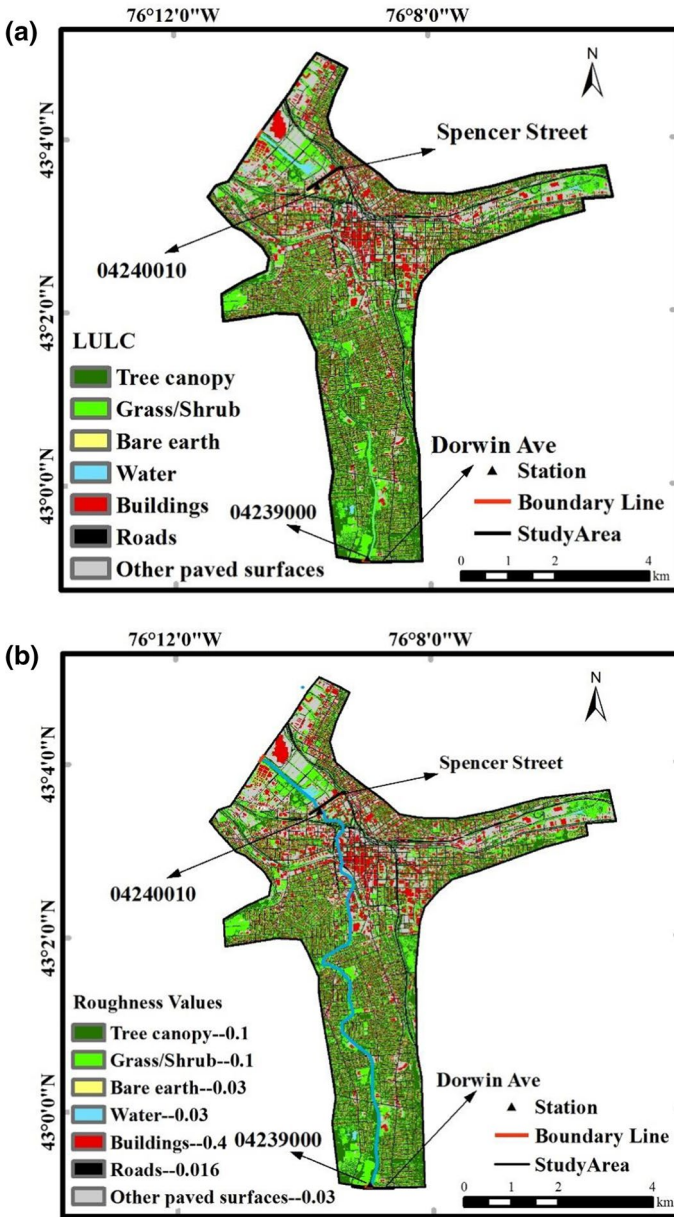
Fig. 3 Spatially distributed values of surface roughness and their original land use/cover (LULC) types. **a** LULC types; **b** values of surface roughness

created to determine flow directions within the 2D simulation domain. In this study, the first one was assured during the construction of 2D DEM data (Fig. 2) and the second was generated by defining that flow only enters the 2D flow area from the upstream boundary and moves out of the study area from the downstream boundary (i.e., the red line in Fig. 2). This

Table 1 The roughness values assigned to all LULC types

LULC types	Tree canopy	Grass/shrub	Bare earth	Water	Roads	Buildings	Other paved surfaces
Roughness value	0.1	0.1	0.03	0.03	0.016	0.4	0.03

definition assumes that even during flood inundation, water overflowing from the channel to the 2D adjacent areas would only flow out of the simulation domain through the downstream boundary, which is reasonable as both sides of the study area have lower elevations than its neighbors and thus water cannot move out from the sides. In the study area, flow hydrograph obtained from the gauging station for a selected storm event was used as the upstream boundary condition, while normal depth as a parameter to be calibrated was used as the downstream boundary. The normal depth assumes that river flows under normal flow (uniform flow) conditions at the downstream boundary of the channel within the study area. It is calculated by HEC-RAS based on a local channel slope input by the user.

2.4 Model calibration

Calibrating the model requires assessing three model parameters. The first is the pre-modeling run time (T). HEC-RAS 2D assumes that the modeled channel at the beginning is dry, which is not realistic. So, the model needs to be run for a period such that channel water depth reaches the beginning water depth of the input hydrograph. There is no general rule available for determining how long this period should be. The second is the normal depth. Its value was initially assigned as the local channel slope near the downstream end of the channel (S_L), which was calculated by extracting from the high-resolution DEM elevation values of a series of points along the channel from the outlet up to a point about 200 m downstream of the USGS gauging station at Spencer street for determining the elevation difference within the length, and then calculating the ratio of the difference to the length. The calculated value of S_L is 0.0014. Whether this value is appropriate needs to be tested. The third is roughness coefficient, n described earlier.

We used a past storm event in 2007 when flows were large enough to cause local limited and isolated inundation sites to calibrate these three types of parameters. As the studied reach has been relatively stable since its channelization, we can assume that channel morphology during this event was similar to that generated from the DEM in this study. After preliminary tests, we found that changing values of T and S_L had minor effects on the modeled water depths, while a small variation of n could lead to higher-degree changes in modeling results. So, we fixed T as 14 h and S_L as 0.0014 and sought for a set of n values that may best predict the measured water depths by comparing modeled and measured water depths using the following three metrics:

- Coefficient of Efficiency (COE), which is defined as

$$COE = \frac{\sum_{i=1}^{n} \left(T_i^p - \overline{\overline{T^m}} \right)^2 - \sum_{i=1}^{n} \left(T_i^p - T_i^m \right)^2}{\sum_{i=1}^{n} \left(T_i^p - \overline{\overline{T^m}} \right)^2} \tag{1}$$

where $\overline{T^m}$ is the mean of measured water discharges and T_i^p and T_i^m are the predicted and measured water discharges, respectively. COE is equivalent to Nash–Sutcliffe index (Nash and Sutcliffe 1970; Cameron et al. 2000) and indicates how well the overall prediction is.

- Normalized Absolute Error (NAE), which is defined as (Smith et al. 2008)

$$NAE = 1 - \frac{\sum_{i=1}^{N} \left| T_i^p - T_i^m \right|}{\sum_{i=1}^{N} \left| T_i^m - \overline{T^m} \right|} \tag{2}$$

- Root Mean Square Error (RMSE), which is defined as

$$RMSE = \sqrt{\frac{1}{n} \sum_{i=1}^{n} \left(T_i^p - T_i^m \right)^2} \tag{3}$$

COE is more affected by the errors for higher values (e.g., peak water depth), while NAE is more influenced by errors for low values (e.g., lower water depths along rising and falling limbs of a hydrograph) (Krause et al. 2005; Montanari 2005). RMSE measures relative accuracy among predictions based on different S_L values. The smaller the RMSE, the better the prediction.

Modeling results based on many sets of n values including the set reported in only three sets may produce reasonably well predictions (Table 2). Overall, they had similar COE and RMSE values, while their NAE values are significantly different from one another. Among them, case 3 predicted the peak water depth closest to the measured one, while their arrival times were similar (Table 2). From the perspective of modeling extreme events, better fitting for high water depths is more important than for lower ones. Therefore, case 3 was better and the associated n values were selected for modeling the projected 500-year flood event.

**Table 2** Calibration of roughness coefficient using a storm event in 2007

	H_{pdiff}*	T_{pdiff}**	COE	NAE	RMSE
Case 1: tree (0.2), water (0.018), same for others	− 3.13%	34.97%	0.6518	0.0023	1.2197
Case 2: tree (0.1), water (0.018), same for others	− 4.20%	30.60%	0.6374	− 0.0847	1.2136
Case 3: tree (0.2), water (0.020), same for others	1.91%	34.97%	0.7114	0.1640	1.2397

* Refers to the difference between measured and modeled peak water depth

**Refers to the difference of the arrival times between measured and modeled peak water depth

Table 3 The five highest flood events in the Onondaga Creek

Rank	Time	Flood stage (m)
1	July 3–5, 1974	1.975
2	June 20–25, 1972	1.890
3	March 5–6, 1979	1.673
4	April 2–4, 2005	1.573
5	March 30–31, 1960	1.542

Fig. 4 Hydrograph of the 1974 storm event and the constructed 500-year hydrograph
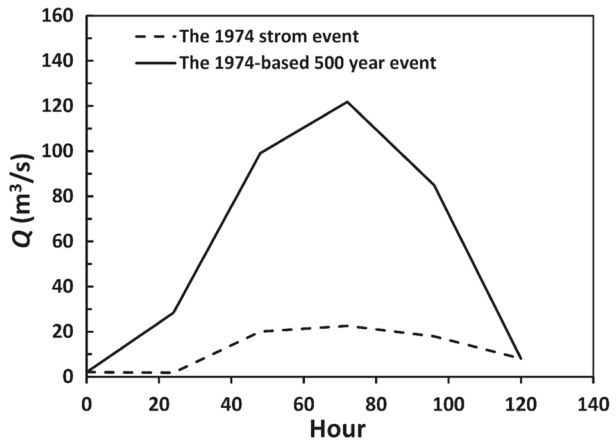
2.5 Simulation of flood inundation due to a projected 500-year storm event

Since a 500-year storm event is an extreme flood event that has not occurred in the Onondaga Creek, its true hydrograph at the upstream boundary of the study reach is unknown. Thus, the shape and magnitude of the hydrograph have to be estimated. We developed a method of constructing this hydrograph by analyzing historical discharge data obtained from the upstream gauging station at Darwin Avenue, which may be described as follow. First, using a series of peak discharges from 1945 to 2016, we performed flood frequency analysis by fitting a Log Pearson Type 3 distribution to the data series and extending the fitted curve to determine the peak discharge of the 500-year event, which is 150.1 m^3/s. Second, we selected five largest flood events based on the hydrological records from 1865 to 2007 (U.S. Army Corps of Engineers 2010) (Table 3) and quantitatively examined their hydrograph. Our examination showed that (a) all events had a relatively steep rising limb and a relatively gentle falling limb and the ratio of the rising time to falling time was 0.33 on average and (b) the inflection point on the rising limbs of the five events was on average associated with the water discharge of about 11.33 m^3/s. Third, based on the results from the first two steps, we selected the hydrograph of the 1974 event (Fig. 4) as the prototype because it had a smooth shape with a single mode and the highest peak discharge. Fourth, this hydrograph was used to construct the hydrograph for the 500-year event following a self-designed procedure: (i) the hydrograph above 11.33 m^3/s was divided into nine segments and the slope of each segment was calculated subsequently; (ii) the peak discharge was increased from the original one (21.5) to 150.1 m^3/s; and (iii) both limbs were raised

by increasing the slopes of the nine segments proportionally and the resulted hydrograph was regarded as representing the 500-year event (Fig. 4). Using this hydrograph and other input parameters, inundation areas at different flooding times were predicted by HEC-RAS. We define the inundation process as that happened in the duration from the beginning of the input 500-year hydrograph to the time when the water depth in a cross section near the outlet is the same as that in the upper boundary at the beginning of the event.

2.6 Analysis of the inundation process and process-based damage assessment

We recorded the simulation results hourly for the created 500-year event and illustrated the dynamic changes of the entire inundation process by selecting three representative inundation moments at the early (the 47th hour), maximum (the 80th hour), and late (the 115th hour) stages. At each selected hour, the inundation depths within the flooded areas were categorized into four classes, in which class 1, 2, 3, and 4 refer to the inundation depths in the 0–1 m, 1–2 m, 2–3 m, and >3 m ranges, respectively. These four classes were also used to denote buildings within these four different ranges of inundation depths. The illustration was followed by further quantitative examination of the temporal changes of the maximum inundation depth and stream power, and inundation area over the inundation process. Moreover, the temporal trends of these three parameters after the end of the inundation process defined in this study were explored to show the full path of the inundation process. Using data in the selected three moments, we then demonstrated quantitatively the variable impact of inundation depths on buildings within the inundation areas by calculating numbers of buildings falling in each of the four classes and their changes over time, and showing their spatial patterns within the inundation areas.

It can be expected that the above-mentioned classification of inundation depths would lead to different results at different moments. To account for this temporal variation, we proposed a new classification that combines inundation depths with their time durations over the entire inundation period. It is quantitatively expressed by the process-based inundation depth (D_{pb}), defined as

$$D_{pb} = \sum_{i=1}^{n} D_i \left(\frac{t_i}{T} \right) \tag{4}$$

where D_i is the inundation depth that lasted for the time period of t_i and T is the entire inundation period. The number of t_i (i.e., n in Eq. (4)) was determined based on the temporal change of D over the entire inundation period. For a given unit inundation area (i.e., 1×1 m^2), D_{pb} reflected the coupled effect of variable D values and their durations and is different from the maximum inundation depth (D_m) in the whole inundation period. The above-mentioned four classes for D_{pb} are referred to as process-based classification (PBC), while those for D_m are denoted as the traditional classification (TC). Using our simulated data, we showed the difference between these two classifications in terms of inundated areas and affected buildings.

This difference showed the complex interaction between inundation depth and duration, which is primarily tied to different land use/cover (LULC) types. Understanding this complexity would reveal the hydrological causes of the differences between PBC and TC and promote use of PBC in other flood-prone regions. To effectively capture the impact of LULC on PBC, the above-mentioned LULC types were merged into three general groups. Group 1 includes trees and grass, group 2 contains bare soils, roads, and bridges, and group

3 involves buildings. For the simulated entire inundation area, A_0, it is easy to establish the following area relationship between PBC and TC:

$$A_0 = A_{n1} + A_{n2} + A_{n3} + A_{n4} = A_{o1} + A_{o2} + A_{o3} + A_{o4} \quad (5)$$

where A_{ni} ($i = 1, 2, 3,$ and 4) is the area of each of the four PBC classes and A_{oi} ($i = 1, 2, 3,$ and 4) is the area of each of the four TC classes. Each area may be further divided into three sub-areas in terms of the three LULC groups. For example, A_{n1} may consist of A_{n11}, A_{n12}, and A_{n13}, while A_{o1} may consist of A_{o11}, A_{o12}, and A_{o13}. Therefore, these relationships may be generally expressed as

$$A_{ni} = A_{ni1} + A_{ni2} + A_{ni3}, \quad i = 1, 2, 3, \text{ and } 4 \quad (6a)$$

$$A_{oi} = A_{oi1} + A_{oi2} + A_{oi3}, \quad i = 1, 2, 3, \text{ and } 4 \quad (6b)$$

Because PBC considered both inundation depths and their associated durations, areas of lower classes in PBC (e.g., A_{n1} and A_{n2}) tended to be greater than those in TC (e.g., A_{o1} and A_{o2}), while the opposite may possibly prevail for higher classes (i.e., A_{o3} and A_{o4}). This means that areas in class 2 of TC (i.e., TC2) may become those either class 1 or 2 in PBC (i.e., PBC1 or 2); areas in class 3 of TC (i.e., TC3) may become those in either class 1, 2, or 3 in PBC (i.e., PBC1, 2, 3); and areas in class 4 of TC (i.e., TC4) may become those in either class 1, 2, 3, or 4 in PBC (i.e., PBC1, 2, 3, or 4). For the three LULC groups, these conversions from TC to PBC may be quantitatively expressed as follow.

For TC2,

$$P_{i-21} + P_{i-22} = \frac{A_{n1i}}{A_{o2i}} + \frac{A_{n2i}}{A_{o2i}} = 1 \quad (7a)$$

For TC3,

$$P_{i-31} + P_{i-32} + P_{i-33} = \frac{A_{n1i}}{A_{o3i}} + \frac{A_{n2i}}{A_{o31}} + \frac{A_{n3i}}{A_{03i}} = 1 \quad (7b)$$

For TC4,

$$P_{i-41} + P_{i-42} + P_{i-43} + P_{i-44} = \frac{A_{n1i}}{A_{o4i}} + \frac{A_{n2i}}{A_{o41}} + \frac{A_{n3i}}{A_{04i}} + \frac{A_{n4i}}{A_{o4i}} = 1 \quad (7c)$$

where $i = 1, 2,$ and 3 denotes each of the three LULC groups and P_* represents the proportion of the area for a given conversion from TC to PBC. Examining the patterns of these P_* may reveal the impact of the three LULC groups on the conversion of areas from TC to PBC.

3 Results

## 3.1 Inundation processes of a 500-year event

Inundation started at the 13th hour in the middle bend and lower straight section of the study reach (Fig. 2). Then, it gradually extended along the channel and the floodplain immediately next to these two sections and reached the maximum extension at approximately the

80th hour. Later, at about the 120th hour, inundated water largely retreated and the in-channel water depth dropped to its original stage. However, water in the inundation zone continuously retreated till about the 144th hour, after which water depths essentially remained unchanged, indicating the end of the flood event (see the inundation video in the supplementary material). Three representative snapshots within the inundation processes (Fig. 5a, b, c) indicated that (i) flood inundation was primarily limited to the neighborhoods close to the channel and in the areas with low elevations and very gentle slopes (i.e., the downstream neighborhoods); (ii) inundation depths varied both spatially at a given moment and temporally from one to another moment; and (iii) spatial variation of inundation depths during the rising limb of the hydrograph (i.e., Fig. 5a) was much greater than that during the falling limb (i.e., Fig. 5c). These visual variations may be further characterized quantitatively.

Since the beginning of flooding, inundation depth increased at an average rate (0.107 m/hr), much higher than that of inundation area (0.063 km^2/hr) within the first 42 h (Fig. 6). In the following 26 h, the increase rate of inundation depth dropped significantly to 0.011 m/hr and that of inundation area was reduced to 0.025 km^2/hr. Both inundation depth and area reached the maximum value at the 80th hour, which was only about 8 h after the arrival time of the peak discharge. Subsequently, inundation depth decreased with a rate of 0.024 m/hr till the end of the event (i.e., the 120th hour). The rate of decrease after the 80th hour was much less than that of increase before the 80th hour for inundation depth, leading to a higher inundation depth of 3.722 m at the 120th hour (Fig. 6). During the same period, inundation area decreased at a rate of 0.043 km^2/hr, which was comparable to the average increase rate before the 80th hour. Yet, at the end of the event, there was still an inundation area of 1.067 km^2. Similar to the change of inundation area, the stream power
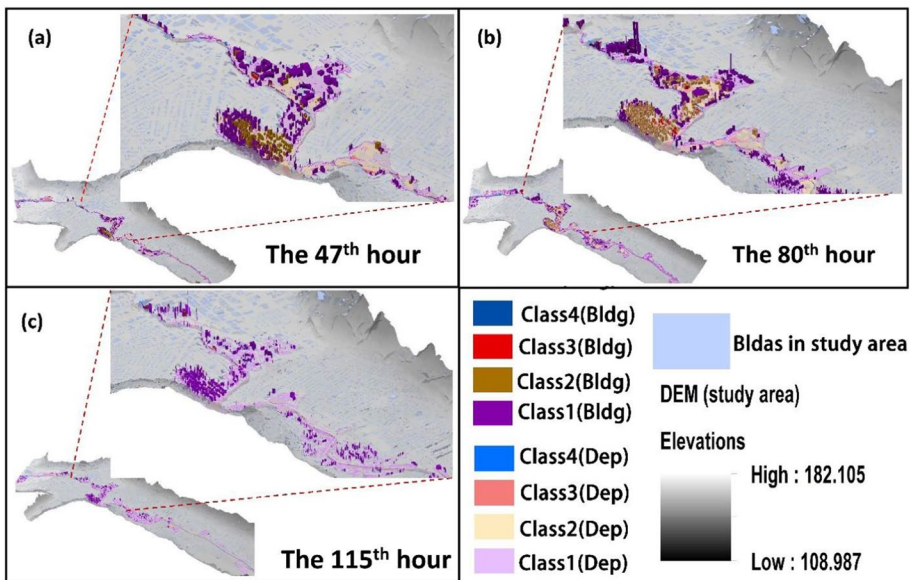
Fig. 5 Three representative moments of the inundation process. In each, blue objects represent buildings within the study area, but outside of the inundation extent; Class 1 (Dep)–Class 4 (Dep) were the four classes of inundation depths; Class 1 (Bldg)–Class 4 (Bldg) were the four classes of buildings falling into the corresponding four classes of inundation depths
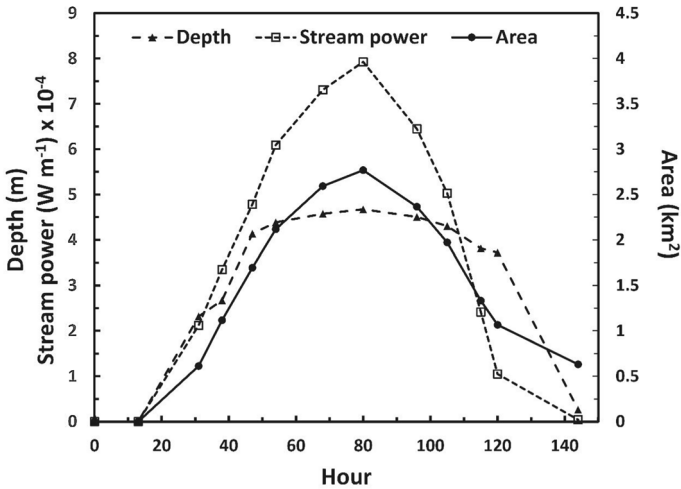
Fig. 6 Temporal changes of the maximum inundation depth, inundation area, and stream power during the entire inundation process

of flooded water increased before the 80th hour and deceased with a similar rate after the 80th hour (Fig. 6). At the end of the event, the remaining flooded water could still have the stream power as high as 1.049×10^{-4} W m^{-1}, indicating that the flooded water was still moving. Although the maximum inundation depth at this moment was 3.722 m, it merely represented 0.02% of the total inundation area (i.e., 1.067 km^2) that had inundation depths greater than 3 m (class 4 in Fig. 7). Those falling in the 2–3 m range took about 3.45% (i.e., class 3 in Fig. 7), while about 22.11% in the 1–2 m range (i.e., class 2 in Fig. 7). The majority of the inundation area had depths ranging between 0 and 1 m (i.e., class 1 in Fig. 7), taking about 74.4% of the total inundation area.

Obviously, at the end of the flood event, the inundation process had not ceased yet. Simulation with extended hours (Fig. 8a) showed that both inundation depth and area continuously decreased after the end of the flood event for about 24 h and then began to level off after the 144th hour. Similarly, stream power decreased to near zero since the 144th hour. These trends signified that inundation processes actually ended at the 144th hour, though water depth in the channel near the outlet of the studied reach dropped to the original stage 24 h earlier. After this moment, there was still the inundated area of about 0.6 km^2 remained. This area included a set of standstill ponds disconnected with one another (Fig. 8b). These detailed inundation processes provided much more information than a single inundation map for understanding the nature of the flooding and the relevant management.

## 3.2 Difference between process-based and classic inundation classifications

The traditional classification (TC) identified the area of 1.404 km^2 whose inundation depths belong to class 1 (Fig. 9a and Table 4). In the process-based classification (PBC), additional areas identified in class 1 were from classes 2, 3, and 4 in TC, taking the area of 0.874, 0.024, and <0.001 km^2, respectively. Consequently, the inundated area in class 1 of PBC increased by 64.2% from 1.404 to 2.301 km^2. The area in class 2 of TC was identified as 0.894 km^2, most of which (about 97.8% was converted into class 1 of PBC (Table 4).
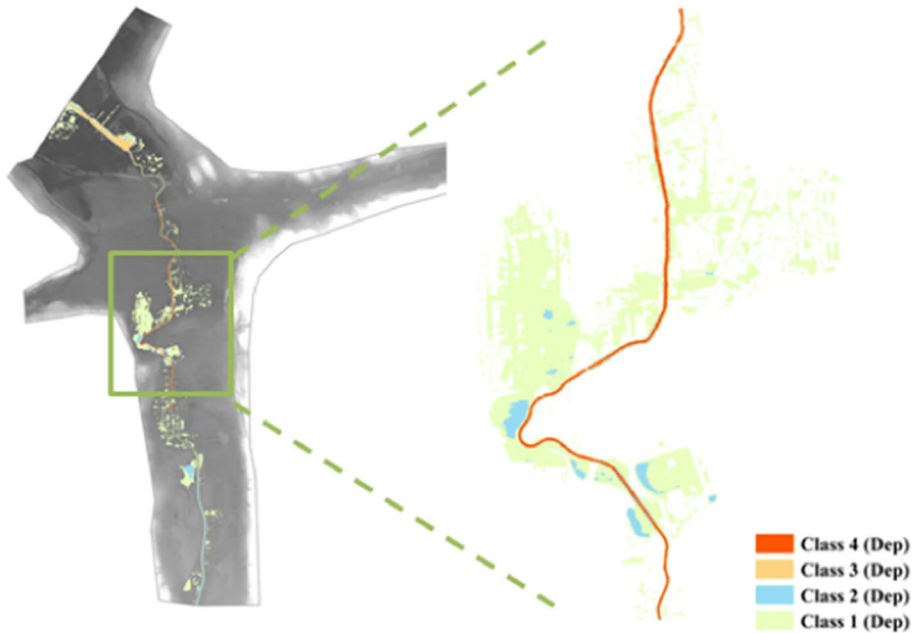
Fig. 7 Spatial distribution of inundation depths at the end of the inundation process (i.e., the 120th hour). The four colors in legend represent the four classes of inundation depths

However, about 88.6% and 17.4% of areas in class 3 and 4 of TC, which make 0.181 and 0.050 km^2, respectively, were converted to the area in class 2 of PBC (Fig. 9a), resulting in the total area of 0.251 km^2 (Table 4). The identified area in class 3 of TC was about 0.205 km^2, whereas in the same class of PBC was around 0.182 km^2, decreased by 11.2%. This decrease was the net effect of two processes. First, the majority of areas in class 3 of TC were transformed to class 1 and 2 of PBC by 0.024 and 0.181 km^2, respectively. Second, a proportion of areas in class 4 of TC, which amounted to 0.182 km^2, was converted to class 3 of PBC (Table 4). The area of class 4 in TC was 0.289 km^2, but decreased to 0.056 km^2 in PBC. The decreased area was mainly transformed into class 3 by 0.182 km^2 and class 2 by 0.05 km^2 (Fig. 9a and Table 4). Overall, the areas in higher classes (i.e., class 3 and 4) of TC significantly shifted to lower classes (i.e., class 1 and 2) of PBC with more areas clustered in class 1 of PBC. This difference between the two different types of classification suggested that inundation depths taking account of inundation dynamics are significantly lower than the static inundation depths.

Numbers of buildings (N_b) falling into the four classes also changed from TC to PBC. The N_b in class 1 was 657 in TC, while it increased to 1146 in PBC (Table 5). The majority of the increased N_b was from class 2 in TC (Fig. 9b), which was 487 (Table 5). The N_b in class 2 was greatly decreased from 496 in TC to 65 in PBC. Most of the decreased N_b (i.e., 487) was transferred to class 1 in PBC (Fig. 9b), though 49 buildings in class 3 and 7 buildings in class 4 of TC were transferred to PBC 2. TC had 51 buildings in class 3, but 49 of them were shifted to class 2 of PBC and only 2 were transferred to class 1. In class 4, most of the 15 buildings of TC were turned into class 3 and 2 evenly with $N_b = 7$, leaving only one building in class 4 (Table 5). Similar to the case of inundated areas, most changes happened in the switch of those in class 2 to class 1 from TC to PBC. In higher classes (i.e., 3
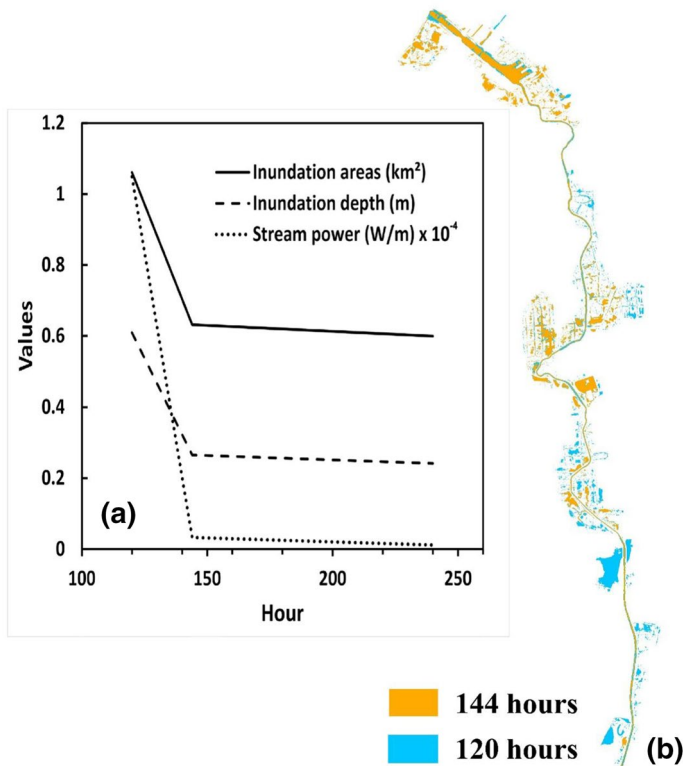
Fig. 8 Development of post-event flood inundation. **a** Temporal trends of the maximum inundation depth, inundation extent, and stream power; **b** comparison of spatially distributed inundation depths between the 120th and 144th hours

and 4), changes of inundated areas were more complex than those of buildings. Nonetheless, both inundated areas and buildings showed a general trend of shifting from high to low classes, reflecting the impact of inundation duration on damage classification.

3.3 Roles of land use/cover in the changing trends between TC and PBC

At the local spatial scale (i.e., the areas surrounding individual buildings), the role of land use and land cover (LULC) in the transfer of inundated areas from TC to PBC was different in different classes. For class 2 of TC, more than 97% of the area in all three LUC types was turned into the area in class 1 of PBC (Fig. 10a), indicating that LULC types did not have impact on the switching of areas from class 2 in TC to class 1 in PBC. Majority of the area in class 3 of TC was turned into class 2 in PBC, such that the converted area for each LULC type of class 2 in PBC took 95.3, 95.2, and 85.4% of that in the original class 3 of TC, respectively (Fig. 10b). Thus, the area in LULC type 3 tended to be less easily transferred to that in class 2 of PBC. In class 4 of TC, 45% and 32% of the area were transferred into that of class 3 and 2 in PBC, respectively, for LULC type 1, whereas 23% of it remained the same class in PBC (Fig. 10c). These three percentages were 47.2, 37.8, and 15% for LULC type 2, while 41.5, 41.5, and 17%

Fig. 9 Difference between process-based (PBC) and classic inundation (TC) classifications for **a** inundation areas and **b** inundated buildings
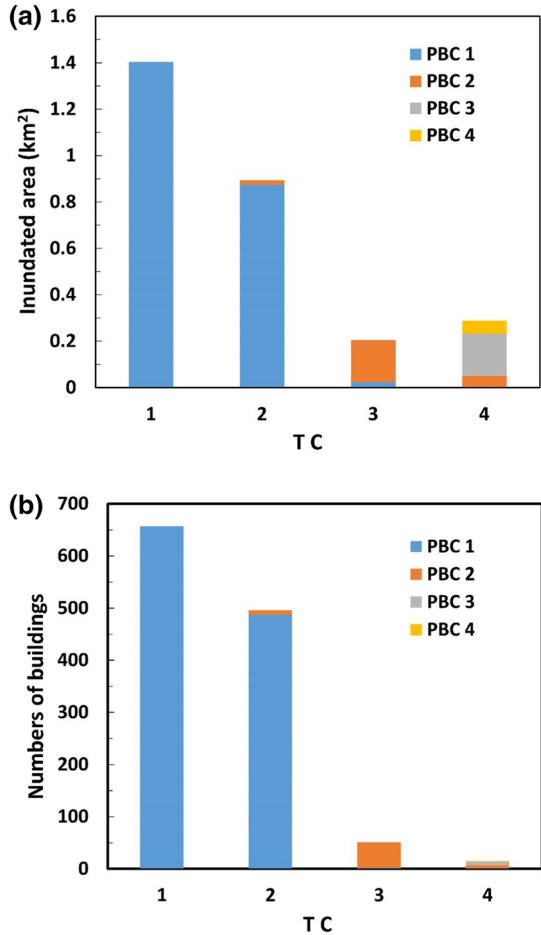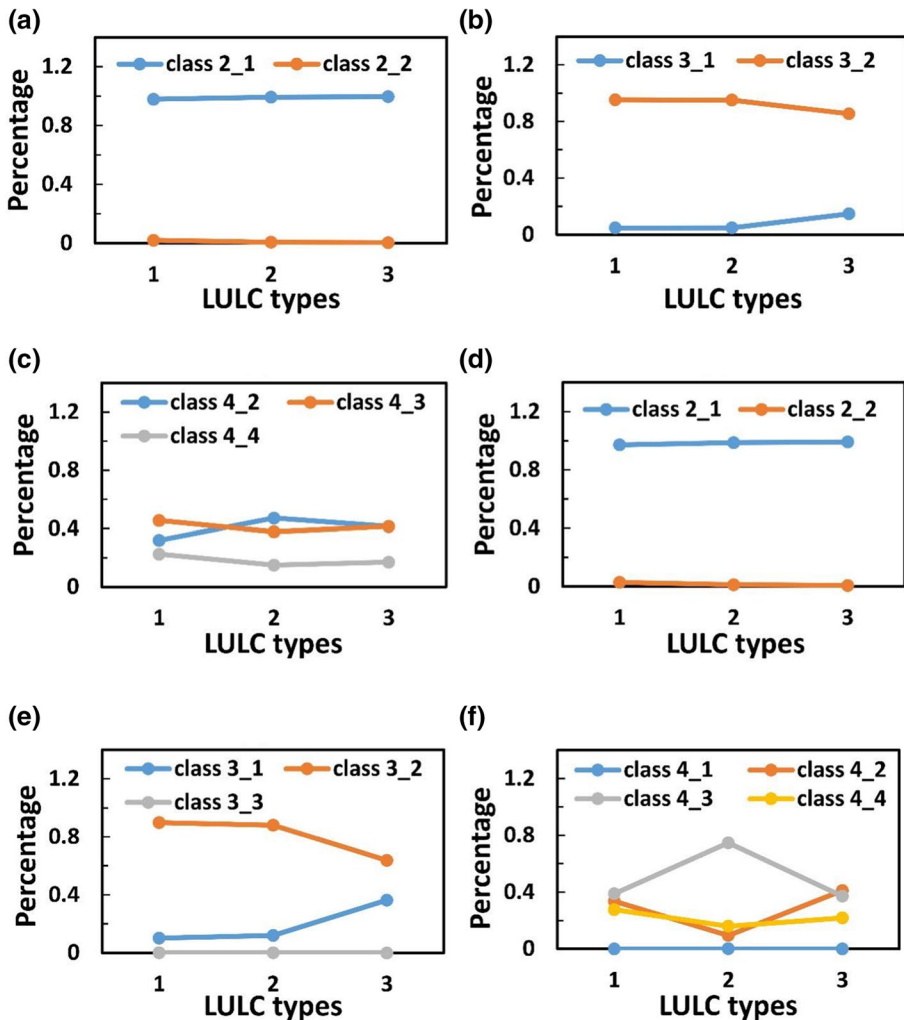

Table 4 Differences of inundation areas between the two classifications (PBC vs TC)

	PBC 1	PBC 2	PBC 3	PBC 4	TC area (km^2)
TC 1	1.4036				1.4036
TC 2	0.8740	0.0197			0.8936
TC 3	0.0236	0.1810	1.545×10^{-4}		0.2047
TC 4	2.997×10^{-5}	0.0503	0.1820	0.0564	0.2888
PBC area (km^2)	2.3012	0.2509	0.1822	0.0564	

for LULC type 3. Thus, more percentages of the area in class 4 of TC were turned into class 2 and 3 of PBC than remained in class 4. Furthermore, LULC type 2 in class 4 of TC tended to be converted into class 2 of PBC easier, whereas LULC type 1 inclined to relatively easy to be switched to LULC type 3 of PBC (Fig. 10c).

Table 5 Differences of inundated buildings between the two classifications (PBC vs TC)

	PBC 1	PBC 2	PBC 3	PBC 4	N_b of TC
TC 1	657				657
TC 2	487	9			496
TC 3	2	49	0		51
TC 4	0	7	7	1	15
N_b of PBC	1146	65	7	1	

Fig. 10 Impact of land use/cover (LULC) on differences of inundated areas between the two types of classification (i.e., PCB vs TC) in different classes. In each figure, class x_y indicates percentage of inundated areas in x class of TC being turned into y class in PBC. For each of LULC types (i.e., the horizontal axis), the sum of percentages of all points equals 1. **a**, **b**, and **c** are for changes of inundated areas around individual buildings, while **d**, **e**, and **f** are for those of inundated areas

At the global spatial scale (i.e., the entire inundated area), LULC types again had no obvious impact on the transfer of the area in class 2 of TC to class 1 of PBC (Fig. 10d). However, their roles become more complex for areas transferred in class 3 and 4 of TC. In class 3 of TC, percentages of areas that remained in class 3 of PBC were almost zero for all three LULC types (Fig. 10e) and hence may be negligible. Although more areas were turned into class 2 of PBC, different percentages of the original areas in the three LULC types were transferred, which were 89.8, 88, and 63.7% for LULC type 1, 2, and 3, This signified that LULC type 1 and 2 were easier to be transferred to class 2 of PBC than LULC type 3. The percentages of transferred areas in class 1 of PBC were also different, showing 10.2%, 12%, and 36.3% for LULC type 1,2, and 3, respectively. This suggested that LULC type 3 was easier to be transferred to class 1 of PBC. In class 4 of TC, the variable percentages of transferred areas for the three LULC types were mainly exhibited in class 2,3, and 4, because little areas were turned into class 1 of PBC (Fig. 10f). For LULC type 1, converted areas in class 2 and 3 of PBC and that remained in class 4 of PBC were similar, taking the percentage of the original area between 28 and 38%. For LULC type 3, percentages of the converted areas to class 2 and 3 of PBC were similar, which were 41% and 37%, respectively, but higher than that remained in class 4 of PBC, which was only 21.9%. Yet, for LULC type 2, 74% of the original area was transferred to class 3 of PBC, while only 9.3% went to class 2 and 15.9% remained in class 4 of PBC. These patterns suggested that in class 4 of TC, LULC type 2 tended to be more readily transferred to class 3 of PBC, LULC type 1 may be prone to stay in the same class (i.e., 4) of PBC, and LULC type 3 did not show significant preference.

4 Discussions

4.1 Modeling uncertainties

Although roughness coefficients for the 500-year event were calibrated using an event in 2007, we have no way to know whether these calibrated values truly represent surface roughness of a 500-year event. To assess this uncertainty in modeling, we run the model using each of the two additionally selected different sets of roughness coefficients, one of which was the best set for a large storm event in 2011. The results showed that compared with the original one (i.e., case 1 in Table 6), increase of roughness coefficients for water bodies by 20% (case 2) and 40% (case 3) would lead to increase of the inundated area by 7.7% and 16.7%, respectively (Table 6). However, the maximum inundation depth almost

Table 6 Model results for the three cases with different roughness coefficients

| Three cases	Roughness coefficients	Maximum inundation area (km^2)	Maximum inundation depth (m)	The arrival time (hour)
Case 1: calibration using the 2007 event	0.2(tree); 0.02(water)	2.7679	5.7789	80
Case 2: the best fit for the 2011 event	0.2(tree); 0.024(water)	2.9826	5.7772	82
Case 3: a different set	0.2(tree); 0.028(water)	3.2307	5.7790	84

remained the same in all three cases, though its arrival time was delayed by 2 and 4 h in case 2 and 3, respectively.

In case 2, the increased 7.7% of inundated areas (i.e., 0.2147 km^2) were mainly concentrated on the very upstream and downstream sections of the study reach (Fig. 11). These two areas were local sinks neighboring the simulated reach (Fig. 2a). In case 3, the additional 9% of inundated areas were created compared with those in case 2. They were located only in the downstream flat area (Fig. 11). Among these additional inundation areas in cases 2 and 3, more than 99% of them had inundation depths in class 1 (i.e., inundation depths range between 0 and 1 m), while less than 1% had inundation depths in class 2 (i.e., between 1 and 2 m). Evidently, changes of roughness coefficients had limited impact on modeling results. Thus, in simulating a 500-year flood event, it is sufficient to 'calibrate' roughness coefficients using a known (relatively) large event. The classic validation step (Horritt 2006; Chen et al. 2015; Yu and Coulthard 2015; Zischg et al. 2018) may not be the best procedure of determining the most appropriate set of roughness coefficients.

4.2 Significance of process-based classification

Given that the simulated flood inundation was a projected 500-year event that has not occurred, there are no measured flood inundation data available for directly validating our calibrated model. Alternatively, we compared our predicted maximum flood inundation map with the latest updated 500-year flood map published by FEMA. Our simulated maximum inundation areas were 51.5% larger than those predicted by FEMA (Fig. 11), apparently representing a significant difference. However, the inundation depths in the overestimated inundated areas were mostly in class 1 (i.e., below 1 m), taking about 89% of the total over-estimated areas (Fig. 12). The remaining 10% and 1% were in classes 2 and 3, respectively. Furthermore, within over-estimated areas in class 1, 23.2%, 15.5%, 6.3%, and 6.5% had inundation depths in the ranges of 0–0.3, 0.3–0.6, 0.6–0.9, and >0.9 m, respectively. This nature of the difference between the two suggested that (1) either model may predict similar inundation areas with higher inundation depths; and (2) FEMA's prediction involved much less inundation areas with smaller inundation depths than ours. The discrepancy in the two predicted inundation areas primarily reflected that considering inundation processes might increase the maximum inundation extent with more areas

Fig. 11 Over-estimation of inundated areas in each class based on classic classification
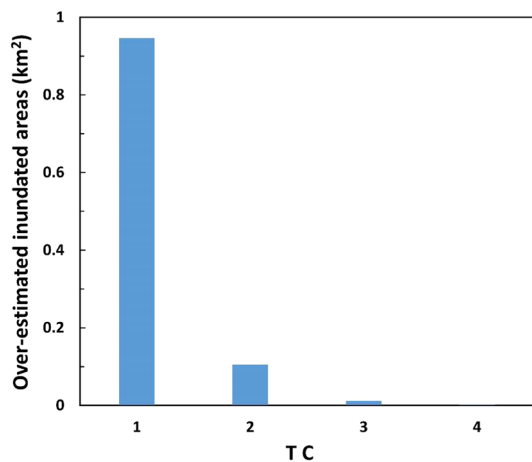
Fig. 12 Comparison of the maximum inundation areas predicted by our model and FEMA. The gray areas were predicted by FEMA; the colored areas were over-predicted areas by our model. The four classes were consistent with those defined earlier based on TC
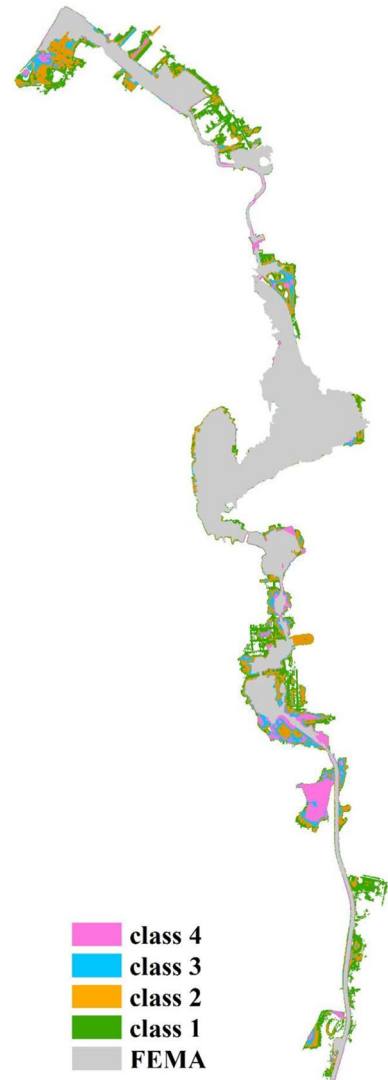
covered by shallow flood water, which could deeply affect existing policies for flood hazard management.

From the perspective of flood management, actions aiming at reducing flood hazard may be taken in three different stages: before, during, or after flooding. Effective spatial plans could be implemented to protect people from being affected by floods before their occurrence (De Moel et al. 2015; O'Grady et al. 2019). Awareness raising and emergency planning are crucial to reduce loss of properties and life during floods (De Moel et al. 2015). Insurance, social safety nets, and entitlement programs can help affect people recover from flood disaster (Blaikie et al. 1994; Cutter et al. 2000; Lamond et al. 2019). Our study contributes to the first two stages. The process-based classification revealed that flood hazard in an urban setting is not only related to the maximum inundation depth, but also affected by inundation duration. This new classification can result in more accurate

and comprehensive flood hazard map for helping emergency planning and rescue work during flooding. It timely ingratiates the growing attention on assessing the complex variability of flood hazard caused by flood dynamics, an issue that has been widely discussed (Costabile et al. 2020; Wu et al. 2020) and provides a practical means of such assessment.

Changes in LULC types have known to affect flood characteristics (Hounkpe et al. 2019). Our analysis further showed that LULC types response differently to flood process. For instance, trees and grass tend to retain water for a longer time period (Fig. 10a–f), suggesting that policies promoting planting trees and grass should be implemented before floods. Therefore, future flood hazard management should be based on the process-based inundation classification as illustrated in this study. Although our findings were based on modeling analysis for a local river, the principle of developing the process-based inundation classification may be easily applied to other rivers for managing extreme floods.

5 Conclusions

Using HEC-RAS 2D, we simulated the flood inundation process of a 500-year event in the downstream reach of Onondaga Creek, located in City of Syracuse, Central New York. Although model results and the subsequent analyses were from a case study, our findings have broad significance for future flood hazard management in other urban settings and are summarized as follows:

(1) Inundation areas and depths and the associated stream powers changed faster during the rising limb than during the falling limb and lasted longer than the duration of the storm event. Associated with these dynamic changes of inundation processes was the fact that number of buildings inundated by flooding water with inundation depths in different ranges (classes) varied from time to time during the entire inundation process. The general implication is that evacuation plan should be implemented as early as possible and flood mitigation management should aim at the period longer than the event duration;

(2) The degree of a building affected by flood inundation is determined not only by inundation depth but also inundation duration. The weighted inundation class quantifying the degree of flood impact on buildings increased generally with inundation duration. Consequently, the degree of flood impact on inundated buildings characterized in terms of the highest inundation depth a building experienced tended to overestimate the flood impact on the building. Assessing flood inundation impact on affected buildings based on the inundation processes is apparently more accurate than that based on the static maximum inundation depths and extent;

(3) For an extreme flood event that has not occurred yet, such as a 500-year event, the classic calibration–validation method for determining model parameters, such as surface roughness (i.e., Manning's n), is not applicable because the true values of surface roughness are unknown. Thus, sensitivity analysis should be a more efficient means of testing robustness of model parameters.

(4) Our modeled maximum inundation extent was slightly larger than that predicted by FEMA with the over-estimated areas mainly occupied by shallow water whose depth less than 0.5 m. This difference more reflected the fact that HEC-RAS 2D accounts for the cumulative effect of inundation processes, while HEC-RAS 1D considers the lumped inundation effect. We propose that future flood control management should

consider the impact of the entire flood inundation processes rather than a static inundation map.

Author contributions PG designed and wrote the paper; WG performed model analysis; and NK performed further model assessment and data analyses.

Declarations

Conflict of interest The authors declare that they have no conflict of interest.

References

Abdessamed D, Abderrazak B (2019) Coupling HEC-RAS and HEC-HMS in rainfall-runoff modeling and evaluating floodplain inundation maps in arid environments: case study of Ain Sefra city, Ksour Mountain. SW of Algeria Environ Earth Sci. https://doi.org/10.1007/s12665-019-8604-6

Adelekan IO (2011) Vulnerability assessment of an urban flood in Nigeria: Abeokuta flood 2007. Nat Hazards 56:215–231. https://doi.org/10.1007/s11069-010-9564z

Afshari S, Tavakoly AA, Rajib MA, Zheng X, Follum ML, Omranian E, Fekete BM (2018) Comparison of new generation low-complexity flood inundation mapping tools with a hydrodynamic model. J Hydrol 556:539–556. https://doi.org/10.1016/j.jhydrol.2017.11.036

Alivio MBT, Puno GR, Talisay BAM (2019) Flood hazard zones using 2d hydrodynamic modeling and remote sensing approaches Global. J Environ Sci Manag-Gjesm 5:1–16. https://doi.org/10.22034/gjesm.2019.01.01

Apel H, Aronica GT, Kreibich H, Thieken AH (2009) Flood risk analyses—how detailed do we need to be? Nat Hazards 49:79–98. https://doi.org/10.1007/s11069-008-9277-8

Aroca-Jimenez E, Bodoque JM, Garcia JA, Diez-Herrero A (2017) Construction of an integrated social vulnerability index in urban areas prone to flash flooding. Nat Hazards Earth Syst Sci 17:1541–1557. https://doi.org/10.5194/nhess-17-1541-2017

Arrault A, Finaud-Guyot P, Archambeau P, Bruwier M, Erpicum S, Pirotton M, Dewals B (2016) Hydrodynamics of long-duration urban floods: experiments and numerical modelling. Nat Hazards Earth Syst Sci 16:1413–1429. https://doi.org/10.5194/nhess-16-1413-2016

Awadallah AG, Tabet D (2015) Estimating flooding extent at high return period for ungauged braided systems using remote sensing: a case study of Cuvelai Basin. Angola Nat Hazards 77:255–272. https://doi.org/10.1007/s11069-015-1600-6

Banks JC, Camp JV, Abkowitz MD (2014) Adaptation planning for floods: a review of available tools. Nat Hazards 70:1327–1337. https://doi.org/10.1007/s11069-013-0876-7

Barredo JI (2007) Major flood disasters in Europe: 1950–2005. Nat Hazards 42:125–148. https://doi.org/10.1007/s11069-006-9065-2

Bisht DS, Chatterjee C, Kalakoti S, Upadhyay P, Sahoo M, Panda A (2016) Modeling urban floods and drainage using SWMM and MIKE URBAN: a case study. Nat Hazards 84:749–776

Blaikie P, Cannon T, Davis I, Wisner B (1994) AT RISK: Natural hazards, people's vulnerability and disasters. Routledge, New York

Bodoque JM, Amérigo M, Díez-Herrero A, García JA, Cortés B, Ballesteros-Cánovas JA, Olcina J (2016) Improvement of resilience of urban areas by integrating social perception in flash-flood risk management. J Hydrol 541:665–676. https://doi.org/10.1016/j.jhydrol.2016.02.005

Borga M, Anagnostou EN, Bloschl G, Creutin J-D (2011) Flash flood forecasting, warning and risk management: the HYDRATE project. Environ Sci Policy 14:834–844

Brunner GW (2016) HEC-RES River Analysis System-User's Manual Version 5.0. US Army Corps of Engineers. Institute for Water Resources. US Army Corps of Engineers, Institute for Water Resources, Hydrologic Engineering Center, Davis, CA

Callow JN, Boggs GS (2013) Studying reach-scale spatial hydrology in ungauged catchments. J Hydrol 496:31–46. https://doi.org/10.1016/j.jhydrol.2013.05.030

Cameron D, Beven K, Naden P (2000) Flood frequency estimation by continuous simulation under climate change (with uncertainty). Hydrol Earth Syst Sci 4:393–405

Chen X, Tian C, Meng X, Xu Q, Cui G, Zhang Q, Xiang L (2015) Analyzing the effect of urbanization on flood characteristics at catchment levels. Proc IAHS 370:33–38

Costabile P, Macchione F (2015) Enhancing river model set-up for 2-D dynamic flood modelling. Environ Model Softw 67:89–107. https://doi.org/10.1016/j.envsoft.2015.01.009

Costabile P, Costanzo C, De Lorenzo G, Macchione F (2020) Is local flood hazard assessment in urban areas significantly influenced by the physical complexity of the hydrodynamic inundation model? J Hydrol 580: https://doi.org/10.1016/j.jhydrol.2019.124231

Cutter SL, Mitchell JT, Scott MS (2000) Revealing the vulnerability of people and places: a case study of Georgetown County. S C Ann as Am Geogr 90:713–737

Darabi H, Choubin B, Rahmati O, Haghighi AT, Pradhan B, Klove B (2019) Urban flood risk mapping using the GARP and QUEST models: a comparative study of machine learning techniques. J Hydrol 569:142–154. https://doi.org/10.1016/j.jhydrol.2018.12.002

De Moel H, Jongman B, Kreibich H, Merz B, Penning-Rowsell E, Ward PJ (2015) Flood risk assessments at different spatial scales. Mitig Adapt Strat Glob Change 20:865–890

DHI (2003) MIKE 11-A Modelling System for Rivers and Channels - User Guide. DHI Water & Environment

Dimitriadis P et al (2016) Comparative evaluation of 1D and quasi-2D hydraulic models based on benchmark and real-world applications for uncertainty assessment in flood mapping. J Hydrol 534:478–492. https://doi.org/10.1016/j.jhydrol.2016.01.020

D'Oria M, Maranzoni A, Mazzoleni M (2019) Probabilistic assessment of flood hazard due to levee breaches using fragility functions. Water Resour Res. https://doi.org/10.1029/2019wr025369

Dormitory Authority of the State of New York (2016) Onondaga Creek Flood and Sediment Study. Department of Environmental Conservation, New York

Dorn H, Vetter M, Hofle B (2014) GIS-based roughness derivation for flood simulations: a comparison of orthophotos. LiDAR Crowdsourced Geodata Remote Sens 6:1739–1759. https://doi.org/10.3390/rs6021739

Dottori F, Todini E (2011) Developments of a flood inundation model based on the cellular automata approach: testing different methods to improve model performance. Phys Chem Earth 36:266–280. https://doi.org/10.1016/j.pce.2011.02.004

Dottori F, Todini E (2013) Testing a simple 2D hydraulic model in an urban flood experiment. Hydrol Process 27:1301–1320. https://doi.org/10.1002/hyp.9370

Fan Y, Ao T, Yu H, Huang G, Li X (2017) A Coupled 1D-2D hydrodynamic model for urban flood inundation. Journal: Advances in Meteorology 2017:Article ID 2819308. https://doi.org/10.1155/2017/2819308

FEMA (2016) Flood Insurance Study-ONONDAGA COUNTY, NEW YORK. Federal Emergency Management Agency, New York

Franci F, Bitelli G, Mandanici E, Hadjimitsis D, Agapiou A (2016) Satellite remote sensing and GIS-based multi-criteria analysis for flood hazard mapping. Nat Hazards 83:S31–S51. https://doi.org/10.1007/s11069-016-2504-9

Gain AK, Hoque MM (2013) Flood risk assessment and its application in the eastern part of Dhaka City. Bangladesh J Flood Risk Manag 6:219–228. https://doi.org/10.1111/jfr3.12003

Gao P, Hartnett JJ (2016) Exploring the causes of an extreme flood event in Central New York. USA Phys Geogr 37:38–55. https://doi.org/10.1080/02723646.2016.1153332

Horritt MS (2006) A methodology for the validation of uncertain flood inundation models. J Hydrol 326:153–165

Hounkpe J, Diekkruger B, Afouda AA, Sintondji LOC (2019) Land use change increases flood hazard: a multi-modelling approach to assess change in flood characteristics driven by socio-economic land use change scenarios. Nat Hazards 98:1021–1050. https://doi.org/10.1007/s11069-018-3557-8

IPCC (2013) Climate Change 2013: The Physical Science Basis Contribution of Working Group I to the Fifth Assessment Report of the Intergovernmental Panel on Climate Change [Stocker, T.F., D. Qin, G.-K. Plattner, M. Tignor, S.K. Allen, J. Boschung, A. Nauels, Y. Xia, V. Bex and P.M. Midgley (eds.)]. Cambridge University Press, Cambridge University Press, Cambridge, United Kingdom and New York, NY, USA, 1535 pp, doi:https://doi.org/10.1017/CBO9781107415324

Jalayer F et al (2014) Probabilistic GIS-based method for delineation of urban flooding risk hotspots. Nat Hazards 73:975–1001. https://doi.org/10.1007/s11069-014-1119-2

Jenkins K, Surminski S, Hall J, Crick F (2017) Assessing surface water flood risk and management strategies under future climate change: Insights from an Agent-Based Model. Sci Total Environ 595:159–168. https://doi.org/10.1016/j.scitotenv.2017.03.242

Jonkman SN (2005) Global perspectives of loss of human life caused by floods. Nat Hazards 34:151–175. https://doi.org/10.1007/s11069-004-8891-3

Krause P, Boyle DP, Base F (2005) Comparison of different efficiency criteria for hydrological model assessment. Adv Geosci 5:89–97

Kvocka D, Falconer RA, Bray M (2015) Appropriate model use for predicting elevations and inundation extent for extreme flood events. Nat Hazards 79:1791–1808. https://doi.org/10.1007/s11069-015-1926-0

Kvocka D, Ahmadian R, Falconer RA (2018) Predicting flood hazard indices in torrential or flashy river basins and catchments. Water Resour Manag 32:2335–2352. https://doi.org/10.1007/s11269-018-1932-6

Lamond JE, Bhattacharya-Mis N, Chan FKS, Kreibich H, Montz B, Proverbs DG, Wilkinson S (2019) Flood risk insurance, mitigation and commercial property valuation. Prop Manag 37:512–528. https://doi.org/10.1108/pm-11-2018-0058

Langhammer J, Vackova T (2018) Detection and mapping of the geomorphic effects of flooding using UAV photogrammetry. Pure Appl Geophys 175:3223–3245. https://doi.org/10.1007/s00024-018-1874-1

Li GF, Xiang XY, Tong YY, Wang HM (2013) Impact assessment of urbanization on flood risk in the Yangtze River Delta. Stoch Environ Res Risk Assess 27:1683–1693. https://doi.org/10.1007/s00477-013-07061

Link O, Brox-Escudero LM, Gonzalez J, Aguayo M, Torrejon F, Montalva G, Eguibar-Galan MA (2019) A paleo-hydro-geomorphological perspective on urban flood risk assessment. Hydrol Process. https://doi.org/10.1002/hyp.13590

Liu DN, Guo XD, Xiao BW (2019) What causes growth of global greenhouse gas emissions? Evidence from 40 countries. Sci Total Environ 661:750–766. https://doi.org/10.1016/j.scitotenv.2019.01.197

Mani P, Chatterjee C, Kumar R (2014) Flood hazard assessment with multiparameter approach derived from coupled 1D and 2D hydrodynamic flow model. Nat Hazards 70:1553–1574. https://doi.org/10.1007/s11069-013-0891-8

Marchi L et al (2009) Comprehensive post-event survey of a flash flood in Western Slovenia: observation strategy and lessons learned. Hydrol Process 23:3761–3770

Marchi L, Borga M, Preciso E, Gaume E (2010) Characterisation of selected extreme flash floods in Europe and implications for flood risk management. J Hydrol 394:118–133. https://doi.org/10.1016/j.jhydrol.2010.07.017

Mason DC, Bates PD, Amico JTD (2009) Calibration of uncertain flood inundation models using remotely sensed water levels. J Hydrol 368:224–236. https://doi.org/10.1016/j.jhydrol.2009.02.034

Meesuk V, Vojinovic Z, Mynett AE, Abdullah AF (2015) Urban flood modelling combining top-view LiDAR data with ground-view SfM observations. Adv Water Resour 75:105–117. https://doi.org/10.1016/j.advwatres.2014.11.008

Meyer V, Scheuer S, Haase D (2009) A multicriteria approach for flood risk mapping exemplified at the Mulde river. Ger Nat Hazards 48:17–39

Mihu-Pintilie A, Cimpianu CI, Stoleriu CC, Perez MN, Paveluc LE (2019) Using high-density LiDAR data and 2D streamflow hydraulic modeling to improve urban flood hazard maps: A HEC-RAS multi-scenario approach. Water. https://doi.org/10.3390/w11091832

Montanari A (2005) Large sample behaviors of the generalized likelihood uncertainty estimation (GLUE) in assessing the uncertainty of rainfall-runoff simulations. Water Resour Res. https://doi.org/10.1029/2004wr003826

Nash JE, Sutcliffe J (1970) River flow forecasting through conceptual models, part I: a discussion of principles. J Hydrol 10:282–290

Onondaga Environment Institute (2009) Onondaga Creek conceptual revitalization plan. Onondaga Environmental Institute, Syracuse, NY

O'Grady MJ, Evans B, Eigbogba S, Muldoon C, Campbell AG, Brewer PA, O'Hare GMP (2019) Supporting participative pre-flood risk reduction in a UNESCO biosphere. J Flood Risk Manag. https://doi.org/10.1111/jfr3.12520

Prabnakorn S, Suryadi FX, Chongwilaikasem J, de Fraiture C (2019) Development of an integrated flood hazard assessment model for a complex river system: a case study of the Mun River Basin. Thail Model Earth Syst Environ 5:1265–1281. https://doi.org/10.1007/s40808-019-00634-7

Rojas R, Feyen L, Watkiss P (2013) Climate change and river floods in the European Union: socio-economic consequences and the costs and benefits of adaptation. Glob Environ Change 23:1737–1751

Roosa MMD, Hartmann TT, Spit TTJM, Johann GG (2017) Constructing risks—internalisation of flood risks in the flood risk management plan. Environ Sci Policy 74:23–29. https://doi.org/10.1016/j.envsci.2017.04.007

Sanders BF, Schubert JE, Gallegos HA (2008) Integral formulation of shallow-water equations with anisotropic porosity for urban flood modeling. J Hydrol 362:19–38. https://doi.org/10.1016/j.jhydrol.2008.08.009

Sarhadi A, Soltani S, Modarres R (2012) Probabilistic flood inundation mapping of ungauged rivers: linking GIS techniques and frequency analysis. J Hydrol 458:68–86. https://doi.org/10.1016/j.jhydrol.2012.06.039

Schumann GJP, Vernieuwe H, De Baets B, Verhoest NEC (2014) ROC-based calibration of flood inundation models. Hydrol Process 28:5495–5502. https://doi.org/10.1002/hyp.10019

Smith P, Beven KJ, Tawn JA (2008) Informal likelihood measures in model assessment: theoretic development and investigation. Adv Water Resour 31:1087–1100. https://doi.org/10.1016/j.advwatres.2008.04.012

Smith MW, Carrivick JL, Hooke J, Kirkby MJ (2014) Reconstructing flash flood magnitudes using "Structure-from-Motion": a rapid assessment tool. J Hydrol 519:1914–1927. https://doi.org/10.1016/j.jhydrol.2014.09.078

Sy B, Frischknecht C, Dao H, Consuegra D, Giuliani G (2019) Flood hazard assessment and the role of citizen science. J Flood Risk Manag. https://doi.org/10.1111/jfr3.12519

Syme WJ (2008) Flooding in urban areas-2D modelling approaches for buildings and fences. In: Proceedings of the Engineers Australia, 9th National Conference on Hydraulics in Water Engineering, Darwin, NT, Australia, September p 23–26

Terti G, Ruin I, Anquetin S, Gourley JJ (2015) Dynamic vulnerability factors for impact-based flash flood prediction. Nat Hazards 79:1481–1497. https://doi.org/10.1007/s11069-015-1910-8

Tsakiris G (2014) Flood risk assessment: concepts, modelling, applications. Nat Hazards Earth Syst Sci 14:1361–1369. https://doi.org/10.5194/nhess-14-1361-2014

U.S. Army Corps of Engineers (2010) The DMA 2000 Hazard Mitigation Plan – Onondaga County, New York. http://www.ongov.net/planning/haz/docs.html (last accessible date: March 10, 2018

Waghwala RK, Agnihotri PG (2019) Flood risk assessment and resilience strategies for flood risk management: a case study of Surat City. Int J Disaster Risk Reduct. https://doi.org/10.1016/j.ijdrr.2019.101155

Wahl T, Jain S, Bender J, Meyers SD, Luther ME (2015) Increasing risk of compound flooding from storm surge and rainfall for major US cities. Nat Clim Chang 5:1093–1097. https://doi.org/10.1038/nclimate2736

Wang YG, Zhang WS, Engel BA, Peng H, Theller L, Shi YY, Hu S (2015) A fast mobile early warning system for water quality emergency risk in ungauged river basins. Environ Model Softw 73:76–89. https://doi.org/10.1016/j.envsoft.2015.08.003

Wu JS, Chen Y, Yang R, Zhao YH (2020) Exploring the optimal cost-benefit solution for a low impact development layout by Zoning, as Well as considering the inundation duration and inundation depth. Sustainability 12. https://doi.org/10.3390/su12124990

Yu DP, Coulthard TJ (2015) Evaluating the importance of catchment hydrological parameters for urban surface water flood modelling using a simple hydro-inundation model. J Hydrol 524:385–400. https://doi.org/10.1016/j.jhydrol.2015.02.040

Yu D, Lane SN (2006) Urban fluvial flood modelling using a two-dimensional diffusion-wave treatment, part 2: development of a sub-grid-scale treatment. Hydrol Process 20:1567–1583. https://doi.org/10.1002/hyp.5936

Zhang S, Pan B (2014) An urban storm-inundation simulation method based on GIS. J Hydrol 517:260–268

Zischg AP, Mosimann M, Bernet DB, Rothlisberger V (2018) Validation of 2D flood models with insurance claims. J Hydrol 557:350–361. https://doi.org/10.1016/j.jhydrol.2017.12.042